Oxygen Evolution Reaction over Catalytic Single-Site Co in Well-Defined Brookite TiO_2 Nanorod Surface

Chang Liu[1, #], Jin Qian[2, #], Yifan Ye[3], Hua Zhou[4], Cheng-Jun Sun[4], Colton Sheehan[1], Zhiyong Zhang[1], Gang Wan[5], Yi-Sheng Liu[3], Jinghua Guo[3], Shuang Li[6], Hye-Young Shin[2], Sooyeon Hwang[6], T. Brent Gunnoe[1], William A. Goddard III[2, *], Sen Zhang[1, *]

[1] Department of Chemistry, University of Virginia, Charlottesville, Virginia 22904, USA;

[2] Materials and Process Simulation Center, California Institute of Technology, Pasadena, California 91125, USA;

[3] Advanced Light Source, Lawrence Berkeley National Laboratory, Berkeley, California 94720, USA;

[4] X-ray Science Division, Advanced Photon Source, Argonne National Laboratory, Lemont, Illinois 60439, USA;

[5] Materials Science Division, Argonne National Laboratory, Lemont, Illinois 60439, USA;

[6] Center for Functional Nanomaterials, Brookhaven National Laboratory, Upton, New York 11973, USA

[#] These authors contributed equally.

*Corresponding Authors:

Email for W.A.G.: wag@caltech.edu; ORCID:0000-0003-0097-5716

Email for S.Z.: sz3t@virginia.edu; ORCID: 0000-0002-1716-3741

Abstract

Efficient electrocatalysts for the oxygen evolution reaction (OER) are paramount to the development of electrochemical devices for clean energy and fuel conversion. However, the structural complexity of heterogeneous electrocatalysts makes it a grand challenge to elucidate surface catalytic sites and OER mechanisms. Here we report that catalytic single-site Co in well-defined brookite TiO_2 nanorod (210) surface (Co-TiO_2) presents turnover frequencies (TOFs) that are among the highest for Co-based heterogeneous catalysts reported to date, reaching 6.6 ± 1.2 s^{-1} and 181.4 ± 28 s^{-1} at 300 and 400 mV overpotentials. Based on grand canonical quantum mechanics (GCQM) calculations and single-site Co atomic structure validated by *in-situ* and *ex-situ* spectroscopic probes, we establish a full description of reaction kinetics for the Co-TiO_2 as a function of applied potential, revealing an adsorbate evolution mechanism for the OER. The computationally predicted Tafel slope and TOFs exhibit exceedingly good agreement with experiment.

The oxygen evolution reaction (OER) is an important reaction and often a limiting step in many electrochemical devices that hold great potential for clean energy conversion and fuel transformation, such as water electrolysers,[1, 2, 3] rechargeable metal-air batteries,[4, 5] and electrochemical synthesisers.[6, 7] There has been extensive effort over past decade for new OER catalysts that exhibit the required activity, durability, and selectivity.[8, 9, 10] Many catalytic materials have been studied with impressive catalytic performances in alkaline electrolytes, including layered double hydroxides,[8, 11, 12] perovskites,[9, 13, 14] spinel metal oxides[15, 16] and carbon materials.[17, 18] However, most heterogeneous catalysts studied thus far have non-uniform physical dimensions (morphology, structure and composition) and surface arrangements (facets), making it difficult to refine the structures of the most active surface catalytic sites to serve as synthetic targets.[12, 17, 19] This same issue has obstructed accurate mechanistic studies that might provide new understanding of OER catalysis to suggest strategies for improved catalysts. Therefore, the two unanswered questions critical to heterogeneous OER catalysis are how to identify and construct well-defined catalytic centers for efficient OER catalysis and how to delineate unambiguously the atomistic mechanism and kinetics for OER and competitive reactions at this center.

Recent advances in full solvent quantum mechanics (QM) and metadynamics [20, 21]methods have made it possible to simulate and determine atomistic reaction mechanisms and free energy reaction barriers (dG*) for electrocatalytic reactions. For example, our QM metadynamics calculations for the oxygen reduction reaction (ORR) on the Pt (111) surface led to a predicted dG* within 0.05 eV of experiment.[22] For the CO reduction reaction (CORR) over Cu (100),[23, 24] our calculations predicted that the difference in the barrier for ethanol production compared to ethene is 0.06 eV, which is in agreement with subsequent experimental validation of 0.066 eV. These calculations established that this level of QM (PBE-D3 flavor of DFT) can achieve an accuracy of 0.05 eV or better in reaction free energy barriers not only in gas-solid interfacial systems,[25, 26, 27] but also in liquid-solid conditions.[23, 28, 29, 30]

However, to correlate directly to experiment, we must describe all reaction steps at the same applied potential, including reactants, transition states, and products. To achieve this, we developed recently the Grand Canonical QM (GCQM) method to keep the applied potential constant rather than the number of electrons as in usual QM.[31] These GCQM methods have been applied to the OER over IrO_2 (110)[29] and Fe doped γ–NiOOH[30] systems, predicting a potential for 10 mA cm^{-2} within 0.05 to 0.10 V of experiment. It has also been used for *in-silico* prediction of new OER catalysts.[32] Despite this progress, the uncertainty of using these theoretical OER results is that we do not have direct experimental evidence on the surface structure of the catalyst.

Herein, we report the seamless integration of controlled synthesis of nanocrystals with well-defined catalytic single-sites and the GCQM calculations demonstrating a detailed validation of the theory against experiment for the kinetics of OER. The model catalyst is Co-doped TiO_2 brookite-phase nanorods (Co-TiO_2) with primarily (210) surface facets. The Co is uniformly doped in the nanorods as single-site substitution and is stable during OER conditions, as indicated by *in-situ* extended X-ray absorption fine structure (EXAFS) and *in-situ* synchrotron radiation X-ray diffraction (SRXRD). These Co-TiO_2 nanorods with Co single-site in the TiO_2 surface deliver OER turnover frequencies (TOFs) of 6.6 ± 1.2 s^{-}

$^{-1}$ and 181.4 ± 28 s^{-1} per site at 300 mV and 400 mV overpotentials, which are very close to the GCQM calculations (13.7 s^{-1} and 307.4 s^{-1}). Moreover, the experimental Tafel slope of 72 mV dec^{-1} agrees with the GCQM prediction (74 mV dec^{-1}), revealing the most favourable adsorbate evolution mechanism (AEM) over the Co single-site. This work highlights the benefits of synthesizing well-defined catalytic single-site over monodisperse nanocrystal surfaces together with GCQM calculations in understanding and verifying the OER kinetics, providing a methodological basis for further fine-tuning electrocatalysts for improved efficiency.

Results

Synthesis and characterization of as-synthesized Co-TiO_2 nanorods

The Co-TiO_2 nanorods were synthesized via the thermal decomposition of titanium chloride ($TiCl_4$) and cobalt oleate precursors in a solution of 1-octadecene (ODE) with the surfactants of oleic acid (OAc) and oleylamine (OAm), according to our previously reported method.[33] During the synthesis at elevated temperatures, as we demonstrated previously, OAc reacts with OAm to release a small amount of water, triggering the controlled hydrolysis of $TiCl_4$ during the reaction, while OAm guides the anisotropic growth of TiO_2 to nanorods.[33] The Co doping level was tuned by the ratio of $TiCl_4$ and cobalt oleate and measured with energy dispersive X-ray spectroscopy (EDS) (**Supplementary Fig. 1**). Formation of the brookite-phase TiO_2 is evidenced from the X-ray diffraction (XRD) pattern with a characteristic brookite (121) peak at 2θ = 30.81° (**Supplementary Fig. 2**, JCPDS No. 29-1360, orthorhombic). Our present synthetic method can yield up to 12% Co dopant level (Co atomic percentage out of all metals) without changing the brookite phase of TiO_2. Transmission electron microscopy (TEM) and scanning TEM (STEM) images (**Fig. 1a**, **Supplementary Fig. 3** and **4**) show that the as-obtained Co-TiO_2 with different Co doping levels exhibit a consistent and uniform nanorod morphology with an average width of 4 ± 0.5 nm and a length of 40 ± 8 nm, similar to undoped TiO_2 nanorods. The high-resolution TEM (HRTEM) image of Co-TiO_2 and Fast Fourier Transformation (FFT) (**Fig. 1b**) suggest that these nanorods are single crystals and grow along the <001> direction with (210) surface at side planes of nanorods. Due to the uniform size and shape, the Co-TiO_2 can be readily assembled into a nanorod array in the liquid-air interface and viewed along the longitudinal direction. We found that the nanorods have a rhombic cross-section shape with an angle of ~ 80°/100°, confirming that the nanorods expose four (210) planes as the side facets (**Fig. 1c**). Such a well-defined surface structure was also observed previously in pure TiO_2 and Fe-doped TiO_2 brookite-phase nanorods.[33]

The uniform distribution of Co dopant in the nanorods was confirmed by the high-angle annular dark field (HAADF) STEM image coupled with electron energy loss spectroscopy (EELS) elemental mapping (**Fig. 1d-f**). The coordination environment of Co dopant was further revealed by the Co K-edge EXAFS. The Fourier-transformed (FT) EXAFS acquired at the Co-TiO_2 sample along with the reference samples are presented in **Fig. 2a**. We found that Co-TiO_2 does not show a peak at 2.17 Å, which is related to the Co–Co bond and can be observed in metallic Co foil. Instead, a peak at 1.56 Å corresponding to the Co–O bond, is clearly observed in the Co-TiO_2 spectrum. This first coordination shell peak is located at a position slightly different with that from CoO, Co_3O_4 and $LiCoO_2$, implying a Co coordination environment

different to these cobalt oxides. This peak may correspond to the Co dopant in the TiO_2, showing the Co-O bonding in the TiO_2 matrix. More obviously, no peak similar to Co-Co pathway in CoO, Co_3O_4 and $LiCoO_2$, typically in the range of 2.1-2.4 Å, is observed in Co-TiO_2 sample. This excludes the possible existence of Co metal and Co oxide secondary phases in the samples, which indicates that Co is distributed in the TiO_2 as single-site substitution (more details are discussed in the *in-situ* EXAFS section).

Electrocatalysis over Co-TiO_2

The Co-TiO_2 dispersion was air-sprayed onto commercial carbon paper (Toray paper) and then annealed at 200 ℃ in air overnight to remove organic ligands before electrochemical study. The OER analysis was carried out in an O_2-saturated 1M potassium hydroxide (KOH) aqueous solution. Linear scan voltammetry (LSV) curves are shown in **Fig. 2b**, indicating much lower onset potential of Co-TiO_2 compared to other catalytic materials (continuous 200 LSV curves are also provided in **Supplementary Fig. 5**). The overpotentials at a current density of 10 mA cm_{Geo}^{-2} and 100 mA cm_{Geo}^{-2} (Geo indicates current density normalized over electrode geometric area) for Co-TiO_2 are 332 mV and 396 mV, respectively, superior to CoO nanoparticles and IrO_2 nanoparticle catalysts with the same loading of active metals. Compared with Co-TiO_2, undoped TiO_2 and carbon paper barely generate current, suggesting that the activity of Co-TiO_2 is exclusively contributed by the Co in the nanorod surface. Among the Co-TiO_2 nanorods with different Co dopant levels, the one with 12% Co exhibited the lowest overpotential (**Supplementary Fig. 6**), possibly due to the highest Co single-site density in the nanorod surface. Therefore, this material is specifically discussed in subsequent sections.

The on-line gas chromatography (GC) analyses showed that the Faradaic Efficiency (FE) for O_2 formation is > 95% on carbon paper supported Co-TiO_2 at a current density of 50 mA cm^{-2}_{Geo}. Even at 100 mA cm^{-2}_{Geo}, the FE for O_2 formation is still > 90% (**Supplementary Fig. 7**). The 42-hour chronoamperometry (CA) test at various potentials demonstrated the high stability of Co-TiO_2, with a slight current density decay observed only at high current density conditions (**Fig. 2c**, **Supplementary Fig. 8**). In another 10-hr CA test at 1.62 V vs. reversible hydrogen electrode (RHE), Co-TiO_2 preserved with 99% of its original current density, while that using CoO and IrO_2 nanoparticles decreases to ~ 65% and 90%, respectively (**Supplementary Fig. 9-11**). In addition, no obvious nanorod morphology change was observed after the OER stability test as shown by HRTEM image in **Fig 2d**, indicating the excellent stability of Co-TiO_2 catalyst.

Co single-site structure during catalysis and intrinsic activity

We employed a suite of spectroscopic probes to confirm the structural stability of Co-TiO_2 catalyst under the OER conditions. *In-situ* SRXRD analysis showed that the brookite phase of TiO_2 is intact under high potentials, without Co phase segregation or TiO_2 phase transition to anatase/rutile (**Fig. 3a**). More importantly, *in-situ* Co K-edge EXAFS spectra, acquired with hard X-ray excitation under the OER conditions, demonstrated that the Co single-site dopant structure can be maintained within Co-TiO_2 (**Fig. 3b** and **Supplementary Fig. 12-17**). **Supplementary Table 1** summarizes the structural details we obtained from high-quality EXAFS spectra for the Co-TiO_2 under catalytic potentials as well as the

pristine TiO_2. The Ti coordination environment (atomic distances and coordination numbers in the first and second coordination shells) is consistent in Co-TiO_2 and TiO_2 samples. Co coordination profiles are not only very close under different electrochemical potentials, but they also match with that of Ti. Specifically, for the first coordination shell, the Co-O bond distance is similar to that of Ti-O in TiO_2, indicating the substitution of Co in the TiO_2. For the second coordination shell, the Co-Ti pathway is consistent with Ti-Ti in TiO_2 and Co-TiO_2, further verifying that Co is present as single-site substitution in the TiO_2 brookite lattice and is preserved under OER potentials.

X-ray absorption spectroscopy (XAS) with soft X-ray excitation was used to probe the electronic structure of the Co-TiO_2 material before and after thermal annealing as well as after electrochemical stability testing. For the as-synthesized Co-TiO_2, Ti L-edge and O K-edge XAS spectra showed typical TiO_2 spectra profiles, meanwhile the Co L-edge XAS spectrum displays a CoO-like profile (**Fig. 3c-e**). It indicates that the Co is doped in the TiO_2 matrix as single-site; however, the Co does not form strong hybridization with the O in the TiO_2 matrix at this stage. Therefore, for the as-synthesized Co-TiO_2 nanorods, the hybridization between Co and O resembled that of CoO, suggesting a 2+ oxidation state for Co that is associated with oxygen vacancy in the crystal. We also found that annealing the sample does not change the electronic structure of the Co-TiO_2, implying that annealing does not provide sufficient driving force to initiate stronger hybridization between Co and O.

Interestingly, a clear change in electronic structure of Co-TiO_2 can be seen after electrochemical testing, as suggested by the changed Co L-edge and O K-edge XAS spectra and the unchanged Ti L-edge spectrum. The unchanged Ti L-edge XAS spectrum (**Fig. 3c**) indicates that the TiO_2 matrix overall remains the same, while the changes in the O K-edge and Co L-edge XAS spectra are an indicator of clearly different hybridization. The O K-edge XAS spectrum (**Fig. 3d** and **Supplementary Fig. 18**) exhibits decreased peaks in the range of 528-538 eV, corresponding to the transition from O 1s to O 2p-transition metal (TM) 3d hybridized state. Since the peak intensity is determined by the occupation of the unoccupied O 2p-TM 3d hybridized orbital, decreased peak intensity indicates the appearance of more 3d electrons in the hybridized orbitals.[34, 35, 36] Given that the Ti L-edge spectrum does not show any obvious difference, the extra accumulated 3d electrons are most likely to be from Co-O hybridization. Meanwhile, the Co L-edge spectrum (**Fig. 3e** and **Supplementary Fig. 18**) also shows a changed profile at 780 eV, confirming a strong Co-O hybridization and an emptier Co 3d orbital. Moreover, it is noteworthy pointing out that the O K-edge spectrum of electrochemically tested sample displays a typical TiO_2 spectrum profile and is different to all the CoO_x species, indicating that Co-O hybridization is determined by the TiO_2 crystal electric field.[37] Thus, we suggest that, driven by electrochemical potential, Co doped in the TiO_2 matrix presents Ti^{4+}-like crystal electric field property and is converted into the higher oxidation state.

Such a clear structure, Co single-site in brookite TiO_2 (210) surface, makes it possible to precisely evaluate the intrinsic activity of catalytic centers. First, we obtained electrochemical active surface area (ECSA) of the Co-TiO_2 catalyst via electrochemical double-layer capacitance measurements (**Methods**, **Supplementary Fig. 19** and **20**). Since the Co-TiO_2 nanorods dominantly expose the (210) plane in the surface and a certain proportion of surface Ti is substituted by Co, we then calculated the surface Co

amount from ECSA, leading to the subsequent analysis of TOFs. Controlling Co doping level at 12% allows the optimization of TOFs, which is slightly higher than that of Co-TiO_2 with lower Co content (**Supplementary Fig. 21**). The experimentally observed TOFs over Co-TiO_2 nanorods (12% Co) are 6.6 ± 1.2 s^{-1}, 34.3 ± 9 s^{-1} and 181.4 ± 28 s^{-1} at overpotentials of 300, 350 and 400 mV, respectively, which are among the highest for Co-based heterogeneous catalysts reported to date (**Supplementary Fig. 22**).

GCQM calculations

We carried out GCQM calculations for the experimentally identified brookite TiO_2 (210) surface with 12.5% Co substitution dopants (Methods section). **Supplementary Fig. 23** shows the constructed three double-layer slab models with inversion-symmetry to avoid net dipoles in the cell. We used a 15 Å vacuum in the Z direction to prevent periodic image interactions. The transition states were calculated using the climbing-image nudge elastic band method and confirmed to have one negative frequency.

There are two types of Ti sites in (210) surface, 5 coordinated and 6 coordinated sites (denoted as 5C and 6C). We found that placing the surface Co at the 5C Ti site, rather than 6C Ti, is more stable by 0.25 eV. In order to determine where to place the 2nd and 3rd layer Co, we examined both the case of the 2nd and 3rd layer Co's connecting directly to the 1st layer via O and the non-connecting case. We found that connecting the Co dopants by O in a line is 0.15 eV more stable than having them separated (**Supplementary Fig. 24**). Our *in-situ* EXAFS analyses suggest that the Co is the single-site substitution in the brookite TiO_2 lattice; however, the two cases of Co single-site substitutes connecting in a line via O and non-connecting Co become indistinguishable in Co K-edge EXAFS, as the second coordination shell in both cases contains identical Co-Co and Co-Ti pathways with the same atomic arrangement and distance (Co-Ti will be primary due to concentration). We believe that these Co lines are likely to be formed at the surface under OER conditions. As revealed by XAS with soft X-ray excitation, Co (2+) is doped in the as-synthesized nanorods coupled with oxygen vacancy and is further converted into the higher oxidation state after electrocatalysis. Along with the increase of Co oxidation state and the elimination of oxygen vacancy in the surface layers at high potentials, the induced Co migration can facilitate the formation of such a Co line structure that is more energetically favourable.

We studied systematically the most stable surface structure, including the oxidation state of Co site and surface H_2O under experimental conditions (pH = 14, various potentials (U)) using slab models of the top three layers (**Supplementary Fig. 25**). We found that the H_2O binds strongly to the surface, with a binding energy of -1.12 eV per water molecule, consistent with previous calculations.[38] At U=1.53 V vs. RHE, all Co in the top three layers of lattice prefers an oxidation state of 4+, leading to a d^5 configuration. This is clearly more stable than cases with Co^{2+} and Co^{3+} which can be created using H interstitial or O vacancy in the lattice, as summarized in **Supplementary Fig. 25g**.

Important for the reaction mechanism, we found that each Co dopant introduces 0.19 unpaired spins on the O bridging Co and Ti, as shown in **Fig. 4**. This radical character motivated us to further investigate the OER mechanism by treating this bridging O as a possible active site, in addition to the Co catalytic site. Previous studies on perovskites suggested that the lattice O can interact with adsorbed OH* to form oxygen vacancy and O_2, leading to a reaction pathway named lattice oxygen mechanism (LOM).[19, 39, 40] For some perovskites, LOM can allow the higher OER activity than the adsorbate evolution mechanism

(AEM),[29, 41] which involves only the metal site and associated H_2O. This previous calculation is based on simple scaling relation rather than calculation of explicit barrier height.[40]

We studied both AEM (blue) and LOM (orange) in our system with barrier heights calculated explicitly, in order to compare directly with our experiments, as shown in **Fig. 4**. We started with one monolayer of explicit H_2O solvent to which one additional H_2O was needed at higher U. The overall half reaction under strong basic condition is $4\ OH^- \rightarrow 2\ H_2O + 4\ e^- + O_2$, and each elementary step is included in **Fig. 4**. The AEM was calculated to be the more favourable reaction pathway for our Co-TiO_2 catalyst, with all favourable intermediate structures labelled. Based on the most favorable reaction pathway, we plotted the free energy landscape in **Fig. 5** at pH=14, as a function of applied potential, U. At potentials between 1.43 V and 1.63 V vs. RHE, the O-O coupling (state 3) was found to be the rate determining step (RDS), leading to a linear Tafel Slope region at this potential range.

Direct Comparison of Tafel Slope and TOFs between QM and Experiment

Our previous studies of OER on IrO_2[29] and on Fe-NiOOH[28] had to assume the surface structure, but for the Co-TiO_2 system we can be confident about the surface structure. In particular we obtained activity per active site in experiment, allowing its direct comparison with the GCQM calculated result.

The GCQM predicted a TOF that is normalized to Co single-site in the surface can be expressed as follows:

$$\mathrm{TOF} = \frac{kT}{h} * \exp\left(-\frac{dG^*}{kT}\right) \qquad (1)$$

where $\frac{kT}{h} = 6.26\times10^{12}\ s^{-1}$, $kT = 0.0257$ eV at 298 K, and dG^* is the calculated to be the free energy difference between the RDS and the resting state. The overall comparison is summarized in **Fig. 6**. At 1.53 V, 1.58 V and 1.63 V (300 mV, 350 mV and 400 mV OER overpotential), TOFs in theory are calculated to be 13.7 s^{-1}, 64.8 s^{-1} and 307.4 s^{-1} per site, presenting an exceedingly good agreement with experiment (6.6 ± 1.2 s^{-1}, 34.3 ± 9 s^{-1} and 181.4 ± 28 s^{-1}, respectively).

The Tafel Slope is sensitive to the reaction pathway and mechanism. **Fig. 6** shows clearly that the most favorable AEM mechanism leads to a Tafel Slope of 74 mV dec^{-1}, which is also highly consistent to the experiment result (72 mV dec^{-1}). In contrast, LOM leads to a reaction rate orders of magnitude smaller with a predicted Tafel slope of 247 mV dec^{-1}, confirming the dominant role of AEM in our Co-TiO_2 system. It is worth noting that although our kinetic study is built on the most energetically favorable structure, such a GCQM approach was also applied to other possible single-site Co configurations which we discussed above, including Co connecting in a line and Co not connected. We concluded that these possible structures with single-site Co in the (210) surface exhibited highly consistent Tafel Slope with the predicted TOFs fluctuated within QM calculation accuracy, further confirming the AEM over our Co single-site catalytic center (Supplementary Methods).

Further extension to other M-TiO_2 (M=Mn, Fe, Co, Ni, Cu) nanorods allows us to understand the general OER kinetics over well-defined single-site electrocatalysts. M-TiO_2 nanorods were readily prepared using

the same approach, leading to consistent surface facet, physical dimension, and M content and atomic arrangement[33] (**Supplementary Fig. 26**). Experimentally, these single-site M exhibited intrinsic activities in the order of Co>Ni>Fe, while Cu- and Mn-TiO_2 displayed negligible activities (**Supplementary Fig. 27**). The experimentally observed TOFs for Ni-TiO_2 and Fe-TiO_2 are 2.4 ± 0.6 s^{-1} and 0.7 ± 0.1 s^{-1} at 350 mV overpotential, and 9.4 ± 1.5 s^{-1} and 1.6 ± 0.2 s^{-1} at 400 mV overpotential, respectively. As shown in **Fig. 7**, our GCQM theoretical results (Tafel Slopes and TOFs) are highly consistent to experimental values. It further indicates that the seamless integration of controlled synthesis and advanced GCQM method leads to a faithful digital twin between experimental observables and theoretical prediction, allowing to validate and predict the well-defined catalytic system's performance and mechanism.

By comparing the free energy landscape of Fe-, Co- and Ni-TiO_2 at the same potential (1.63 V), we found that the O-O coupling step and the resting state {the fully covered H_2O state on Co and Ni (state 1), but OH covered on Fe (state 2), see **Supplementary Fig. 28**} control the overall kinetics of our single-site catalysts. Single-site Co provides a favorable combination of these steps, avoiding the resting state energy trap observed in Fe as well as the high deprotonation barrier over Ni (state 1 to state 2), which makes Co-TiO_2 to be the most efficient among these well-defined M-TiO_2 nanorods. It also suggests that the screening of these initial OER steps over a broad range of Co single-site catalytic centers with different inorganic solid coordination environment (e.g., different TiO_2 crystal phases and surface facets)[53], coupled with controlled synthesis, will likely enable the further optimization of OER catalysts.

Conclusions

Using a model catalyst with well-defined Co catalytic single-site, we demonstrated a methodological advance for the study of OER by combining the atomic-precision synthesis of nanocrystals and GCQM calculations. Our synthetic strategy of TiO_2 nanorods with substitutional Co-doping incorporates Co single-site into the brookite-phase TiO_2 (210) surface. The resultant Co-TiO_2 nanorods are highly efficient in catalyzing the OER under basic condition, and these materials are stable against phase transition or segregation under the reaction conditions, as revealed by *in-situ* and *ex-situ* spectroscopic studies. Based on the well-characterized structure, our GCQM calculations provide an atomistic understanding of the OER kinetics in excellent agreement with experiment. With the accuracy of GCQM calculations validated here, it can potentially allow us to perform high-accuracy *in-silico* design of rational catalyst and subsequently maximize its benefit through controlled synthesis of nanocatalysts.

Methods

Chemicals and materials. Titanium chloride ($TiCl_4$, 99%) was purchased from Fluka Analytical. Cobalt carbonyl ($Co_2(CO)_8$, stabilized in 1.5% hexane) was obtained from Stream Chemical Inc. 1,2,3,4-tetrahydronaphthalene (Tetralin, 98%), 1-octadecene (ODE, 90%) and cobalt chloride hexahydrate ($CoCl_2 \cdot 6H_2O$, 98%) were purchased from Acros Organics. Dioctylamine (97%), oleylamine (OAm, 70%) and oleic acid (OAc, 90%) were purchased from Sigma Aldrich. Hexane, isopropanol, and potassium hydroxide (KOH) were purchased from Fisher Scientific. Toray carbon paper 060, plain carbon cloth and Iridium oxide (IrO_2) were obtained from Fuel cell store.

Synthesis of Co-TiO_2, Ni-TiO_2, Fe-TiO_2, Cu-TiO_2, Mn-TiO_2 and TiO_2 nanorods. TiO_2 and Co-TiO_2 nanorods were synthesized via an organic solution colloidal approach, based on our previous publication.[33] As $TiCl_4$ is highly sensitive to moisture, all the solvents employed in the synthesis are pre-dried at 90°C by vacuum using a typical Schlenk link technique. For the synthesis of TiO_2 nanorods, a Ti-precursor solution containing 0.2 M of $TiCl_4$ and 1.0 M of OAc was first prepared by dissolving 2.19 mL of $TiCl_4$ and 31.59 mL of OAc in 66.25 mL of ODE, and was stored in a N_2-filled glovebox. In a four-neck reactor, 10 mL of ODE, 10 mL of OAm and 0.48 mL of OAc were heated under vacuum at 90 °C for one hour to remove dissolved moisture and oxygen, and were subsequently cooled down to 60 °C under N_2. 1.5 mL of the Ti-precursor solution was then injected into the system, which was quickly heated up to 290 °C and maintained at that temperature for 10 min. Next, 8 mL of additional Ti precursor solution was added into the reactor at a rate of 0.3 mL min^{-1}. After cooling down to room temperature, the TiO_2 nanorods were collected and washed by the addition of isopropanol and centrifugation at 8000 rpm for 8 min. The product was further purified twice by the addition of hexanes and isopropanol. The Co-TiO_2 nanorods were synthesized via a similar route. A Co-oleate solution containing 0.2 M of cobalt oleate and 1.0 M of OAc was mixed with the Ti-precursor solution with a desired Ti/Co ratio. 1.5 mL of the mixed solution was injected into the degassed solution containing 10 mL of ODE, 10 mL of OAm, and 0.48 mL of OAc at 60°C, and was quickly heated up to 290°C. After being held at that temperature for 10 min, another 8 mL of the Ti-Co mixed precursor solution was introduced into the system at 0.3 mL min^{-1}. The as-prepared Co-TiO_2 nanorods were collected and purified in the same way for TiO_2 nanorods. In this synthesis, the Co doping level was tuned by altering Ti/Co ratio in the mixed precursor solution. In specific, with the Ti/Co molar ratio of 8/1, 8/2, and 8/3, a Co doping level of 4.2%, 7.5%, 12% can be achieved in the Co-TiO_2 nanorods. Ni-TiO_2, Fe-TiO_2, Cu-TiO_2 and Mn-TiO_2 nanorods were synthesized with the same approach, using the corresponding metal-oleate to substitute for Co-oleate.[33] The synthesis of CoO nanoparticles is described in the Supplementary Methods.

Structural characterizations. XRD patterns were collected using a Rigaku Smartlab diffractometer with Cu Kα radiation (λ=1.5418Å). TEM images were obtained on a FEI Spirit (120 kV). To obtain the TEM image of nanorod array viewed along longitudinal direction, the assembly method should be used, which is described in detail in the Supplementary Methods. HRTEM and STEM images were collected from a FEI Talos 200x (200kV) coupled with EELS and EDS detectors, in the Center for Functional Nanomaterials at Brookhaven National Lab. The EELS mappings and spectra were collected using a high resolution Gatan-Enfina ER with a probe size of 1.3Å. A power law function was used for EELS background subtraction. EDS was collected on a FEI Quanta 650 scanning electron microscope (SEM).

Electrocatalytic OER measurement. All electrocatalysis studies were performed at room temperature in the O_2-saturated 1.0 M KOH electrolyte, using a typical three-electrode system that is controlled by a Bio-Logic (Model VMP3) potential station, with a carbon paper working electrode, a Pt foil counter electrode, and a Hg/HgO (1.0 M KOH) reference electrode. To prepare the Co-TiO_2 working electrode, a desired amount of Co-TiO_2/hexanes dispersion was airbrushed onto carbon paper with a catalyst loading of 4 mg cm^{-2}, followed by annealing at 200 °C overnight to remove the organic ligands. The electrode was then sealed with epoxy with an exposing geometric area of 1 cm^2. The CoO nanoparticle electrode and IrO_2

electrode were also prepared using the same airbrushing technique, except that the Vulcan-72 carbon supported CoO and commercial IrO_2 were dispersed in isopropanol. All the potentials were reported vs. RHE using equation:

$$E(\text{vs. RHE}) = E(\text{vs. HgO}) + 0.926\ \text{V} \quad (2)$$

where 0.926 V is the potential difference between the Hg/HgO (1.0 M KOH) reference electrode and RHE in 1.0 M KOH that is calibrated via open circuit voltage test prior to the electrocatalysis. The overpotential (η) for OER could be calculated using

$$\eta = E(\text{vs. RHE}) - 1.23\ \text{V} \quad (3)$$

The OER activity was examined by linear scan voltammogram (LSV) from 0.926 – 1.676 V vs. RHE at a scan rate of 10 mV s^{-1} with iR compensation. The uncompensated resistance was measured with potentiostatic electrochemical impedance spectroscopy (PEIS) method at a single-point high frequency (100 kHz). The fixed potential was set to 0 V versus open circuit voltage (E_{OCV}) with a sinus amplitude of 20 mV and a delay of 0.1 period. Each test was repeated for 4 measures for averaging the values. The uncompensated resistance (R_u) in our typical cell was around 2 Ohms. IR drop was compensated at 85 % by Bio-Logic EC-Lab software with positive feedback. The catalytic stability was evaluated by Chronoamperometry (CA) measurement at various potentials without iR correction.

To gain a deeper understanding in the OER kinetics, we calculated the electrochemical surface area (ECSA) using the equation

$$ECSA = C_{dl}/C_s \quad (4)$$

where C_s is the specific capacitance of Co-TiO_2 obtained from GCQM calculation under the operando conditions (18.2 μF cm^{-2}, see Supplementary Methods), and C_{dl} is double layer capacitance measured by cyclic voltammetry (CV) in the non-Faradaic region (0.526 – 0.726 V vs. RHE). The amount of Co atoms in nanorod surface ($N_{Co\text{-}atom}$) was estimated by the ECSA and Co atom density in Co-TiO_2 nanorods, which is described by the following equation

$$N_{Co\text{-}atom} = ECSA \times \frac{8 \times w\%}{D_{cell}} \quad (5)$$

where 8 is the number of Ti atoms in single cell of brookite TiO_2, w is atomic ratio of Co element in Co-TiO_2, and D_{cell} is the dimension of (210) facet in a single cell of TiO_2 (2.26×10^{-10} mol cm^{-2}). Based on $N_{Co\text{-}atom}$, the experimental turnover frequency (TOF) is calculated by

$$TOF = \frac{j_{Geo} \times s}{4 \times N_{Co-atom} \times F} \quad (6)$$

where j_{Geo} is geometric current density obtained from LSV plot, s is electrode geometric area, and F is Faraday constant.

To obtain the Faradic efficiency (FE) towards OER, a controlled current electrolysis for 12.5 hour was performed in a gas-tight H-type cell that was separated by a Nafion-212 membrane and charged with 10

mL of N_2-saturated 1M KOH in each compartment. During the electrocatalysis, a steady N_2 supply of 10 sccm was introduced to the anode compartment, and the gas-phase effluent was continuously delivered to the gas-sampling loop of a gas chromatograph (Shimadzu, GC 2014) and analyzed by a thermal conductivity detector (TCD). The concentration of O_2 was derived by comparing the corresponding peak are of TCD with that of standards, which was further used to calculate the FE.

XAS characterization. The *ex-situ* and *in-situ* Co K-edge extended X-ray absorption fine structure (EXAFS) were collected at room temperature in the fluorescence mode at the beamline 20BM of Advanced Photon Source, at the Argonne National Laboratory using a customized electrochemical cell that is detailed in our previous publication.[42] For *in-situ* Co K-edge EXAFS analyses, a desired amount of Co-TiO_2 was airbrushed on the carbon cloth and annealed at 200°C for 12 hours to serve as the working electrode, while a Ag/AgCl and a Pt wire were employed as the reference and counter electrodes, respectively. The CV was conducted at 100 mV min^{-1} with continuous fresh electrolyte (1.0 M KOH) pumping at a rate of 1.0 ml min^{-1}. The processing of EXAFS raw data (background-subtraction, normalization, and Fourier transformation by standard procedures) was performed by the ATHENA program. The least-squares curve fitting analysis of the EXAFS χ(k) data was conducted by the ARTEMIS program. The model was built with substitution of central atom Ti in brookite phase TiO_2 with Co atom. The functions the effective curved-wave backscattering amplitude ($F_j(k)$), the photoelectron mean free path for all paths in Å (λ) and phase shifts ($\phi_j(k)$) were calculated by the ab initio code FEFF 9.05. Soft X-ray XAS were collected at the beamline 8.0.1 in the Advanced Light Source, Lawrence Berkeley National Lab. The signals were collected via total electron yield, measuring the drain current from the ground. The energy scale of each spectrum was calibrated using the reference samples. The processing of soft-XAS raw data (background-subtraction, and normalization) was performed by the ATHENA program.

SR-XRD characterization. *In-situ* SR-XRD measurement for Co-TiO_2 was conducted at the beamline 17BM (λ = 0.24141 Å) of Advanced Photon Source, at the Argonne National Laboratory using the same setup described in the *in-situ* EXAFS characterization. The two-dimensional diffraction patterns were collected with a PerkinElmer Si flat panel detector, which was set 200 mm behind the sample, and were then processed using GSAS-II software to obtain plots of intensity vs. 2θ.

GCQM calculations. All QM calculations used the spin-polarized PBE exchange correlation functional along with the DFT-D2[43] pair potential London dispersion corrections as implemented within the VASP package.[44] To locate the transition states for the various reaction steps, we used the climbing image-nudged elastic band (CI-NEB) method, as implemented in VASP.[45] K-point grid is 2x3x1 and the energy cutoff is 500 eV for all calculations. We group the 5 coordinated Ti/Co and 6 coordinated Ti/Co as one double layer, so that the unit cell has 3 double-layer. The calculated water binding energy on brookite TiO_2 (210) surface is 1.12 eV, which compares well with 6 double-layer result of 1.1 eV reported in literature[38].
To convert from QM energies to Gibbs free energy at 298 K, we calculated phonon vibrational density of states using Density Functional Perturbation Theory (DFPT).[46] The vibrational contributions to free energies have been included for both surfaces and molecules. To compute free energy change of elementary reaction steps involving gaseous or liquid molecules, such as water and hydrogen, we

considered the contributions of rotation, translation, and vibration[47] to the free molecule, which we obtained from Jaguar package[48] as well as the solvation energy of water molecule in liquid water (2.05 kcal/mol). The free energy of gas phase O_2 is derived as

$$G[O_2] = 4.92(eV) + 2G[H_2O] - 2G[H_2] \quad (7)$$

by utilizing experimental Gibbs free energy of the reaction ($2H_2O(l) \rightarrow O_2(g)+2H_2(g)$) at the standard conditions. To obtain the free energies as a function of applied potential, U, we used the CANDLE[49] implicit solvation model as implemented in JDFTx.[50] This has been used successfully for previous OER studies, including IrO_2,[29] Fe doped γ-NiOOH[30] and other metals doped into NiOOH.[32]

We calculated the geometries using VASP with the VASPsol[51] solvation model for various numbers of charges on the surface, then we transformed to the grand canonical potential kinetics (GCP-K)[52] formulation along with the CANDLE implicit solvation model to obtain the free energies as a function of U. This allows the charged surfaces to be effectively screened by the ionic response in solution. A specific example of such a transformation is provided in Supplementary Method. This GCQM calculation was also used for Ni-TiO_2 and Fe-TiO_2 with the same structure, surface facet and reaction condition. The atomic coordinates of the optimized models are provided in **Supplementary Data 1**.

Data Availability

All data generated or analysed during this study are included in this published article (and its Supplementary Information files) or can be obtained from the corresponding authors upon reasonable request.

Code Availability

All computational structures are included in this published article (and its Supplementary Data and Supplementary Information files). The code and script for GCQM computation and analysis are provided as part of the jDFTx constant charge calculations and can be accessed at http://jdftx.org/index.html or can be obtained from the corresponding authors upon reasonable request.

References:

McCrory, C. C. L. et al. Benchmarking hydrogen evolving reaction and oxygen evolving reaction electrocatalysts for solar water splitting devices. *J. Am. Chem. Soc.* **137** 4347-4357 (2015).

Spanos, I. et al. Standardized benchmarking of water splitting catalysts in a combined electrochemical flow cell/inductively coupled plasma–optical emission spectrometry (ICP-OES) setup. *ACS Catal.* **7**, 3768-3778 (2017).

Liu, B. et al. Large-scale synthesis of transition-metal-doped TiO_2 nanowires with controllable overpotential. *J. Am. Chem. Soc.* **135**, 9995-9998 (2013).

An, L. et al. Heterostructure-promoted oxygen electrocatalysis enables rechargeable zinc–air battery with neutral aqueous electrolyte. *J. Am. Chem. Soc.* **140**, 17624-17631 (2018).

Li, Y. et al. Advanced zinc-air batteries based on high-performance hybrid electrocatalysts. *Nat. Commun.* **4**, 1805 (2013).

Liu, J. et al. Metal-free efficient photocatalyst for stable visible water splitting via a two-electron pathway. *Science* **347**, 970-974 (2015).

Wang, H. et al. Bifunctional non-noble metal oxide nanoparticle electrocatalysts through lithium-induced conversion for overall water splitting. *Nat. Commun.* **6**, 7261 (2015).

Burke, M. S., Kast, M. G., Trotochaud, L., Smith, A. M. & Boettcher, S. W. Cobalt–iron (oxy)hydroxide oxygen evolution electrocatalysts: the role of structure and composition on activity, stability, and mechanism. *J. Am. Chem. Soc.* **137**, 3638-3648 (2015).

Seitz, L. C. et al. A highly active and stable $IrO_x/SrIrO_3$ catalyst for the oxygen evolution reaction. *Science* **353**, 1011-1014 (2016).

Zhang, B. et al. Homogeneously dispersed multimetal oxygen-evolving catalysts. *Science* **352**, 333-337 (2016).

Chen, J. Y. C. et al. Operando analysis of NiFe and Fe oxyhydroxide electrocatalysts for water oxidation: detection of Fe^{4+} by mössbauer spectroscopy. *J. Am. Chem. Soc.* **137**, 15090-15093 (2015).

Liu, W. et al. Amorphous Cobalt–iron hydroxide nanosheet electrocatalyst for efficient electrochemical and photo-electrochemical oxygen evolution. *Adv. Funct. Mater.* **27**, 1603904 (2017).

Kim, J., Chen, X., Shih, P.-C. & Yang, H. Porous Perovskite-type lanthanum cobaltite as electrocatalysts toward oxygen evolution reaction. *ACS Sustainable Chem. Eng.* **5**, 10910-10917 (2017).

Suntivich, J., May, K. J., Gasteiger, H. A., Goodenough, J. B. & Shao-Horn, Y. A perovskite oxide optimized for oxygen evolution catalysis from molecular orbital principles. *Science* **334**, 1383-1385 (2011).

Wu, T. et al. Iron-facilitated dynamic active-site generation on spinel $CoAl_2O_4$ with self-termination of surface reconstruction for water oxidation. *Nat. Catal.* **2**, 763-772 (2019).

Li, C. et al. Phase and composition controllable synthesis of cobalt manganese spinel nanoparticles towards efficient oxygen electrocatalysis. *Nat. Commun.* **6,** 7345 (2015).

Gupta, S. et al. Highly active and stable graphene tubes decorated with FeCoNi alloy nanoparticles via a template-free graphitization for bifunctional oxygen reduction and evolution. *Adv. Energy Mater.* **6**, 1601198 (2016).

Toma, F. M. et al. Efficient water oxidation at carbon nanotube–polyoxometalate electrocatalytic interfaces. *Nat. Chem.* **2**, 826-831 (2010).

Roy, C. et al. Impact of nanoparticle size and lattice oxygen on water oxidation on $NiFeO_xH_y$. *Nat. Catal.* **1**, 820-829 (2018).

Laio, A. & Parrinello, M. Escaping free-energy minima. *Pro. Natl Acad. Sci.USA.* **99**, 12562-12566 (2002).

Iannuzzi, M., Laio, A. & Parrinello, M. Efficient exploration of reactive potential energy surfaces using Car-Parrinello molecular dynamics. *Phy. Rev. Lett.* **90**, 238302 (2003).

Cheng, T. et al. Mechanism and kinetics of the electrocatalytic reaction responsible for the high cost of hydrogen fuel cells. *Phys. Chem. Chem. Phys.* **19**, 2666-2673 (2017).

Cheng, T., Xiao, H. & Goddard, W. A. Reaction Mechanisms for the electrochemical reduction of CO_2 to CO and formate on the Cu(100) surface at 298 K from quantum mechanics free energy calculations with explicit water. *J. Am. Chem. Soc.* **138**, 13802-13805 (2016).

Cheng, T., Xiao, H. & Goddard, W. A. Full atomistic reaction mechanism with kinetics for CO reduction on Cu(100) from ab initio molecular dynamics free-energy calculations at 298 K. *Pro. Natl Acad. Sci.USA.* **114**, 1795-1800 (2017).

Qian, J., An, Q., Fortunelli, A., Nielsen, R. J. & Goddard, W. A. Reaction mechanism and kinetics for ammonia synthesis on the Fe(111) surface. *J. Am. Chem. Soc.* **140**, 6288-6297 (2018).

Qian, J. et al. Initial steps in forming the electrode–electrolyte interface: H_2O adsorption and complex formation on the Ag(111) surface from combining quantum mechanics calculations and ambient pressure X-ray photoelectron spectroscopy. *J. Am. Chem. Soc.* **141**, 6946-6954 (2019).

Ye, Y. et al. Dramatic differences in carbon dioxide adsorption and initial steps of reduction between silver and copper. *Nat. Commun.* **10**, 1875 (2019).

Cheng, T., Wang, L., Merinov, B. V. & Goddard, W. A. Explanation of dramatic pH-dependence of hydrogen binding on noble metal electrode: greatly weakened water adsorption at high pH. *J. Am. Chem. Soc.* **140**, 7787-7790 (2018).

Ping, Y., Nielsen, R. J. & Goddard, W. A. The reaction mechanism with free energy barriers at constant potentials for the oxygen evolution reaction at the IrO_2 (110) surface. *J. Am. Chem. Soc.* **139**, 149-155 (2017).

Xiao, H., Shin, H. & Goddard, W. A. Synergy between Fe and Ni in the optimal performance of (Ni,Fe)OOH catalysts for the oxygen evolution reaction. *Pro. Natl Acad. Sci.USA.* **115**, 5872-5877 (2018).

Sundararaman, R., Goddard, W. A. & Arias, T. A. Grand canonical electronic density-functional theory: algorithms and applications to electrochemistry. *J. Chem. Phys.* **146**, 114104 (2017).

Shin, H., Xiao, H. & Goddard, W. A. In silico discovery of new dopants for Fe-doped Ni oxyhydroxide ($Ni_{1-x}Fe_xOOH$) catalysts for oxygen evolution reaction. *J. Am. Chem. Soc.* **140,** 6745-6748 (2018).

Zhang, Z. et al. Generalized synthetic strategy for transition-metal-doped brookite-phase TiO_2 nanorods. *J. Am. Chem. Soc.* **141,** 16548-16552 (2019).

Ye, Y. et al. X-ray spectroscopies studies of the 3d transition metal oxides and applications of photocatalysis. *MRS Commun.* **7,** 53-66 (2017).

Ye, Y. et al. Strong O 2p–Fe 3d hybridization observed in solution-grown hematite films by soft X-ray spectroscopies. *J. Phys. Chem. B* **122,** 927-932 (2018).

Kronawitter, C. X. et al. Electron enrichment in 3d transition metal oxide hetero-nanostructures. *Nano Lett.* **11,** 3855-3861 (2011).

Li, J. et al. Tracking the local effect of fluorine self-doping in anodic TiO_2 nanotubes. *J. Phys. Chem. C* **120,** 4623-4628 (2016).

Holmström, E. et al. Hydration Structure of Brookite TiO_2 (210). *J. Phys. Chem. C* **121,** 20790-20801 (2017).

Grimaud, A. et al. Activating lattice oxygen redox reactions in metal oxides to catalyse oxygen evolution. *Nat. Chem.* **9,** 457 (2017).

Yoo, J. S., Rong, X., Liu, Y. & Kolpak, A. M. Role of Lattice oxygen participation in understanding trends in the oxygen evolution reaction on perovskites. *ACS Catal.* **8,** 4628-4636 (2018).

Rossmeisl, J., Qu, Z. W., Zhu, H., Kroes, G. J. & Nørskov, J. K. Electrolysis of water on oxide surfaces. *J. Electroanal. Chem.* **607,** 83-89 (2007).

Zhang, Z. et al. Revealing structural evolution of PbS nanocrystal catalysts in electrochemical CO_2 reduction using in situ synchrotron radiation X-ray diffraction. *J. Mater. Chem. A* **7,** 23775-23780 (2019).

Grimme, S. Semiempirical GGA-type density functional constructed with a long-range dispersion correction. *J. Comput. Chem.* **27,** 1787-1799 (2006).

Kresse, G. & Furthmüller, J. Efficient iterative schemes for ab initio total-energy calculations using a plane-wave basis set. *Phys. Rev. B* **54,** 11169-11186 (1996).

Henkelman, G., Uberuaga, B. P. & Jónsson, H. A climbing image nudged elastic band method for finding saddle points and minimum energy paths. *J. Chem. Phys.* **113,** 9901-9904 (2000).

Baroni, S., de, G. S., Dal, Corso. A. & Giannozzi, P. Phonons and related crystal properties from density-functional perturbation theory. *Rev. Mod. Phys.* **73,** 515-562 (2001).

Sprowl, L. H., Campbell, C. T. & Árnadóttir, L. Hindered translator and hindered rotor models for adsorbates: partition functions and entropies. *J. Phys. Chem. C* **120,** 9719-9731 (2016).

Bochevarov, A. D. et al. Jaguar: A high-performance quantum chemistry software program with strengths in life and materials sciences. *Int. J. Quantum Chem.* **113,** 2110-2142 (2013).

Sundararaman, R. & Goddard, W. A. The charge-asymmetric nonlocally determined local-electric (CANDLE) solvation model. *J. Chem. Phys.* **142,** 064107 (2015).

Sundararaman, R. et al. JDFTx: software for joint density-functional theory. *SoftwareX* **6,** 278-284 (2017).

Mathew, K., Sundararaman, R., Letchworth-Weaver, K., Arias, T. A. & Hennig, R. G. Implicit solvation model for density-functional study of nanocrystal surfaces and reaction pathways. *J. Chem. Phys.* **140,** 084106 (2014).

Huang, Y., Nielsen, R. J. & Goddard, W. A. Reaction mechanism for the hydrogen evolution reaction on the basal plane sulfur vacancy site of MoS_2 using grand canonical potential kinetics. *J. Am. Chem. Soc.* **140,** 16773-16782 (2018).

Li, X., Rong, H., Zhang, J., Wang, D. & Li, Y. Modulating the local coordination environment of single-atom catalysts for enhanced catalytic performance. *Nano Res.* **13**, 1842–1855 (2020).

Acknowledgements

This work was supported by U.S. National Science Foundation (CBET-1805022, CBET-2004808 and CBET-2005250). This research used resources of the Advanced Photon Source, an Office of Science User Facility operated for the U.S. Department of Energy (DOE) Office of Science by Argonne National Laboratory, and was supported by the U.S. DOE under Contract No. DE-AC02-06CH11357, and the Canadian Light Source and its funding partners. This research used resources of the Center for Functional Nanomaterials, which is a U.S. DOE Office of Science Facility, at Brookhaven National Laboratory under Contract No. DE-SC0012704. This research used resources of the Advanced Light Source, a U.S. DOE Office of Science User Facility under contract no. DE-AC02-05CH11231.

Author Contributions

The project was conceived by C.L. and J.Q. under the supervision of T.B.G., W.A.G. and S.Z.. Catalyst synthesis, structural characterization, and catalysis measurement were performed by C.L., C.S., and Z.Z.. GCQM calculations were finished by J.Q. and H.Y.S.. *In-situ* XRD and *in-situ* EXAFS experiments were conducted by C.L., H.Z., C.-J.S., Z.Z., and G.W.. Soft XAS experiment were conducted by Y.Y., Y.S.L., and J.G.. STEM elemental mapping was done by S.L. and S.H.. The analysis and interpretation of all spectra were done by C.L., Z.Z., and Y.Y.. All authors contributed to the writing of the manuscript.

Competing Interests

The authors declare no competing interest.

Figures

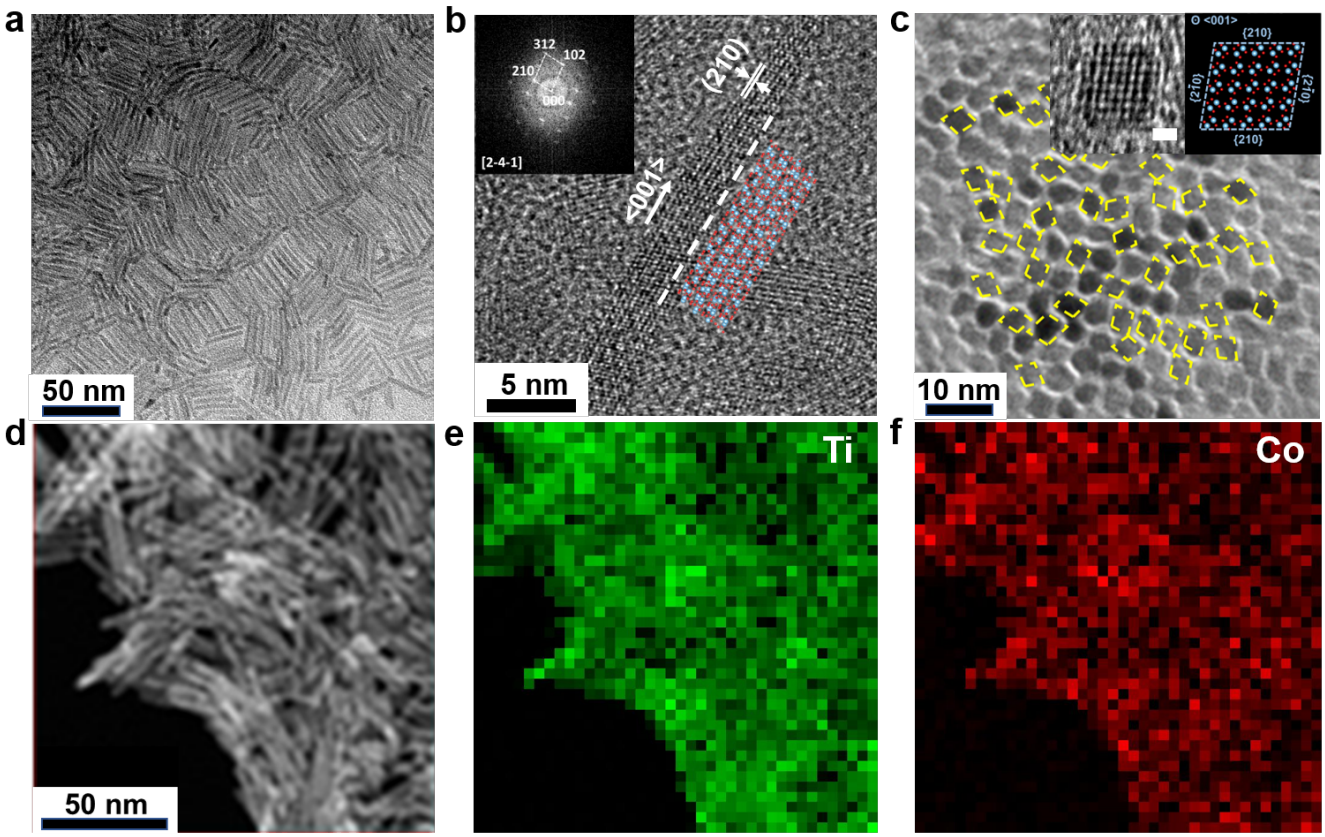

Figure 1. Morphology and structure characterizations of Co-TiO_2 nanorods. a, TEM image of as-synthesized Co-TiO_2 nanorods (12% Co). **b**, Representative HRTEM image of Co-TiO_2 nanorods (inset is FFT). **c**, TEM image of vertically aligned Co-TiO_2 nanorod assembly viewed along longitudinal direction. The inset shows a representative HRTEM image of vertically aligned nanorod. **d**, dark-field STEM image of Co-TiO_2. **e-f**, Ti and Co EELS elemental mapping in the area of d. The atomic model illustrations in (b) and (c) are brookite-phase TiO_2 with blue and red circles being Ti and O.

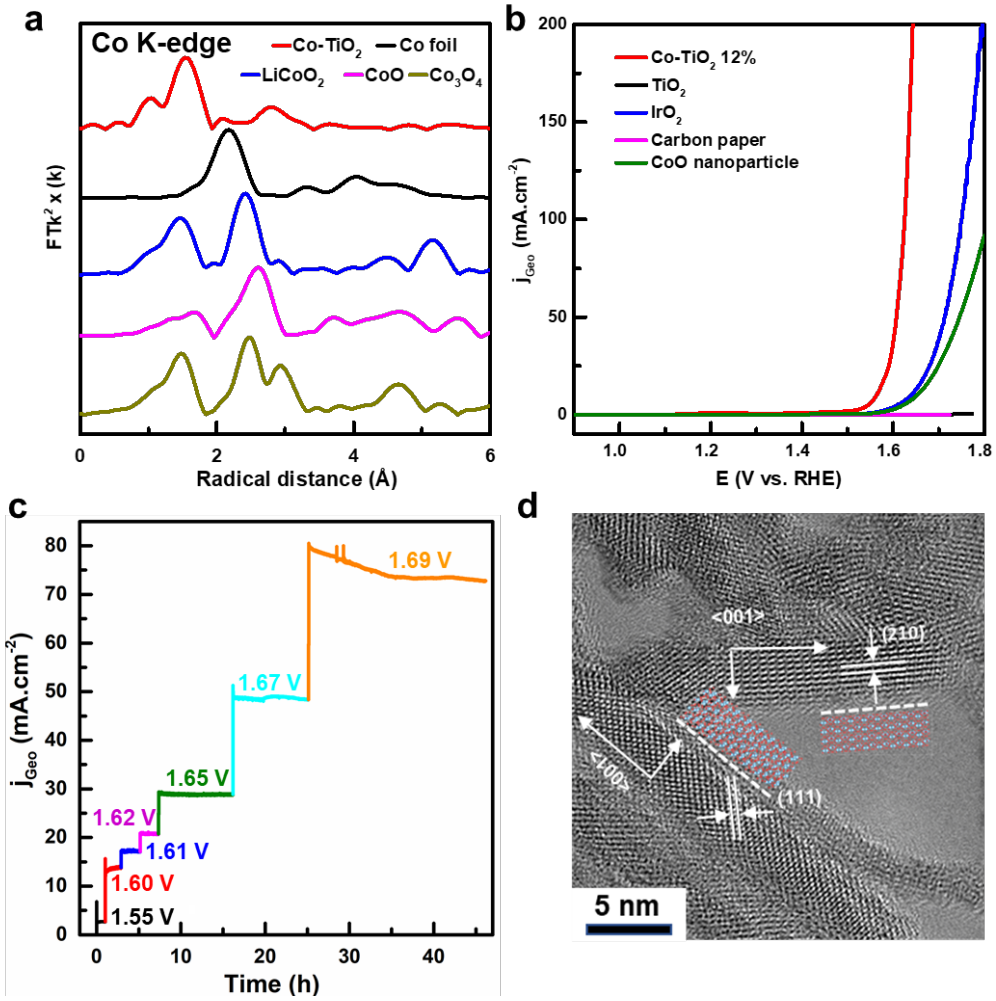

Figure 2. EXAFS and OER catalytic performance of Co-TiO_2 nanorods. a, Co K-edge FT-EXAFS of Co-TiO_2 (12% Co) and other reference materials. **b**, LSV plot of different catalysts for the OER. **c**, OER stability analyses of Co-TiO_2 (12% Co) with chronoamperometry tests under various potentials (the segment color code matches with the applied potential value). **d**, HRTEM image of Co-TiO_2 nanorods after OER stability test. The atomic model illustrations in d are brookite-phase TiO_2 with pale blue and red circles being Ti and O.

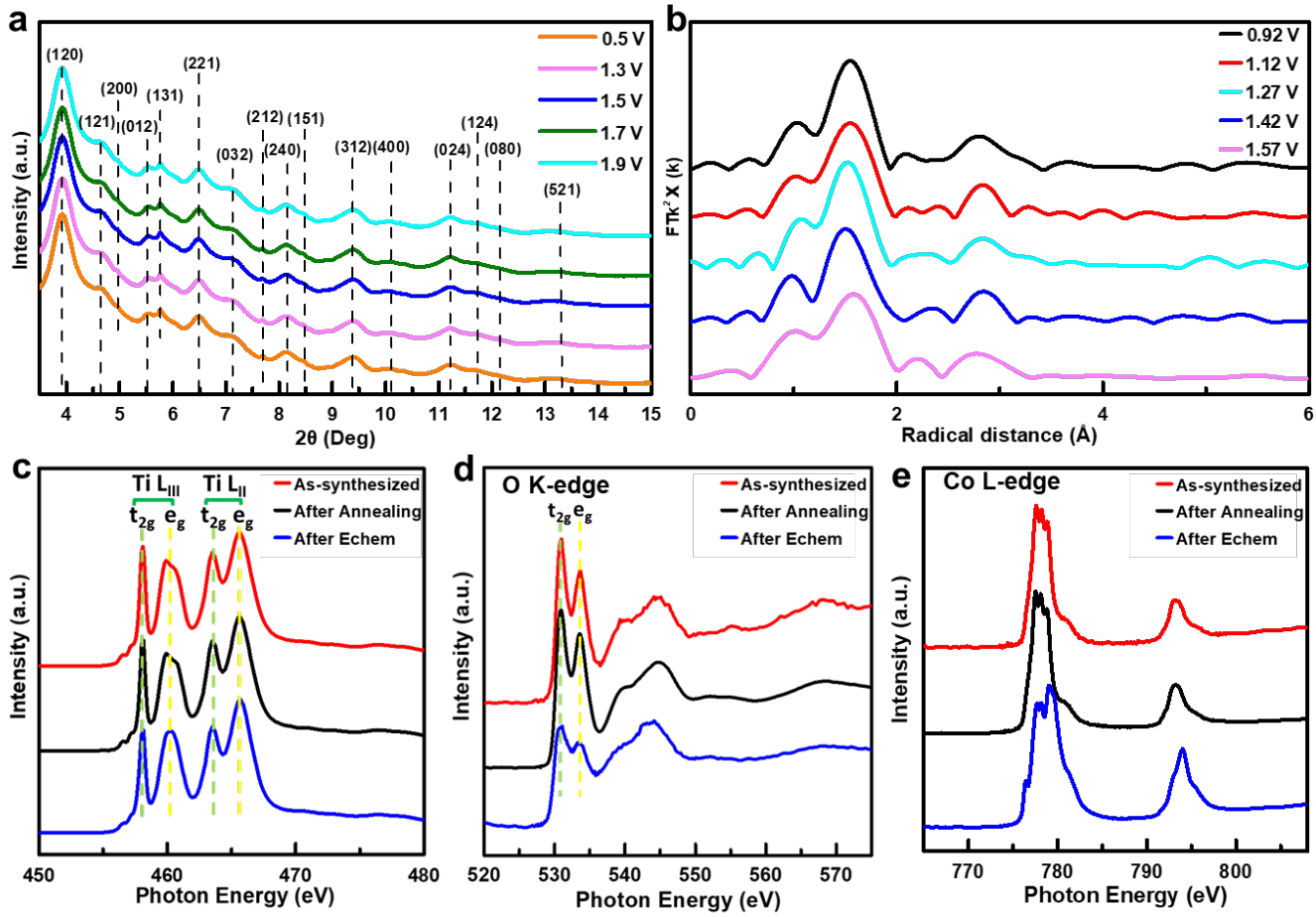

Figure 3. *In-situ* and *ex-situ* analyses of Co-TiO_2. a, In-situ SRXRD patterns of Co-TiO_2 nanorod catalysts under the OER conditions (1M KOH aqueous electrolyte). **b**, *In-situ* Co K-edge FT-EXAFS spectra of Co-TiO_2 nanorods under the OER conditions (1M KOH aqueous electrolyte). **c-e**, Ti L-edge (c), O K-edge (d) and Co L-edge (e) XAS with soft X-ray excitation for Co-TiO_2 nanorods catalysts before and after annealing and after electrochemical testing.

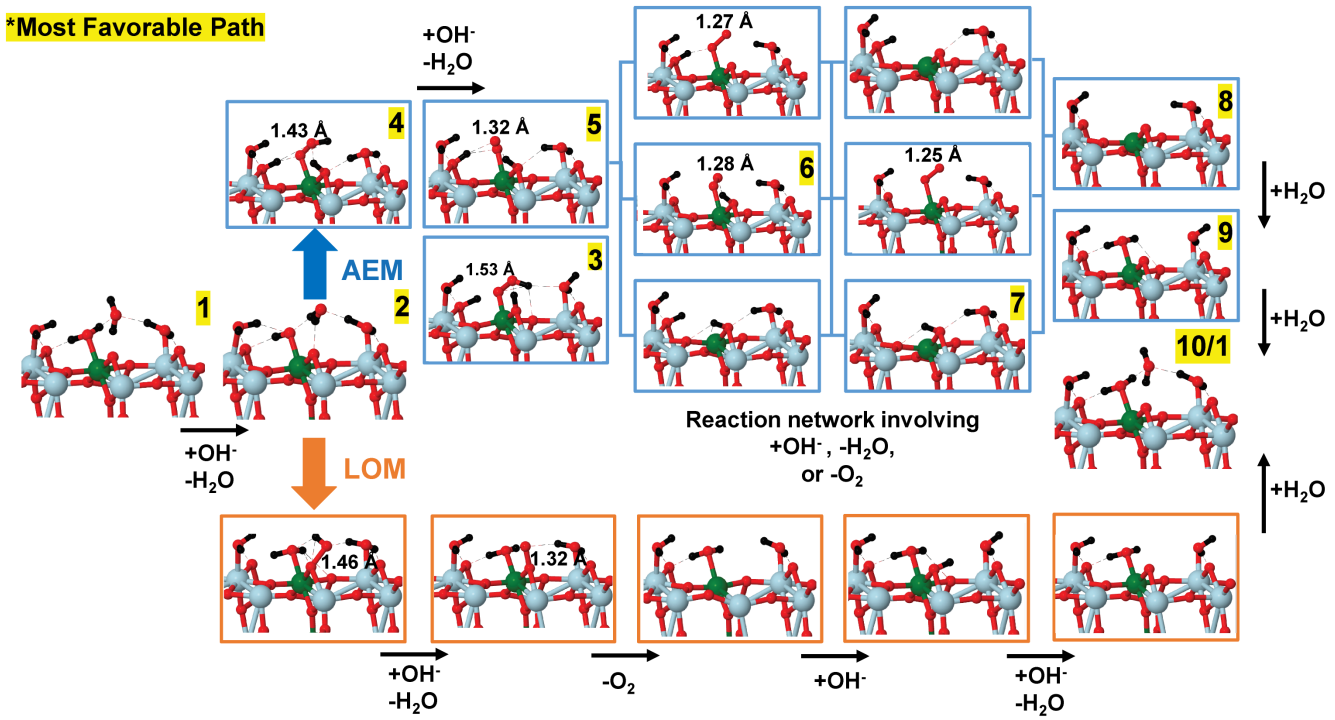

649

650 **Figure 4. Schematic illustration of possible OER reaction mechanisms over Co-TiO_2.** The blue is
651 adsorbate evolution mechanism (AEM) pathway; the orange is lattice oxygen mechanism (LOM) pathway.
652 The States 1-10 are the most energy favorable and are also used in Fig. 5. The green, blue, red and black
653 spheres in atomic models represent Co, Ti, O and H atoms, respectively.

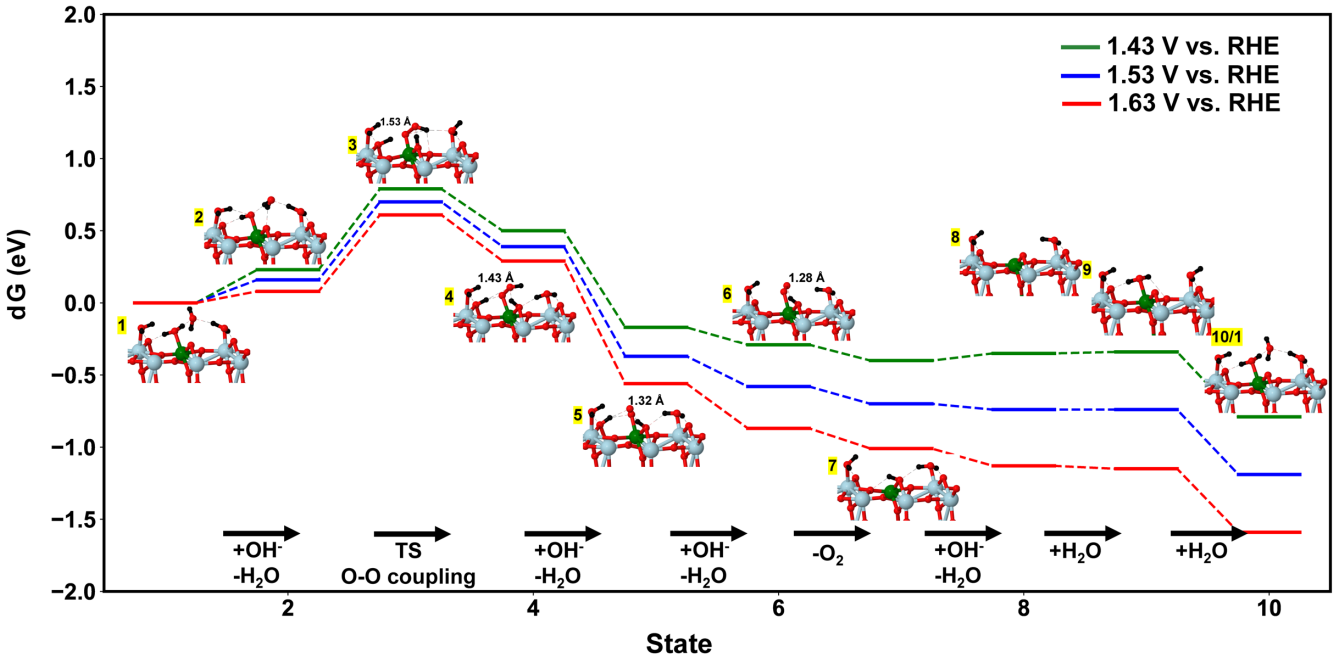

654

Figure 5. Free energy landscape of Co-TiO_2 for different states at pH=14 and different potentials. The green, blue, red and black spheres in atomic models represent Co, Ti, O and H atoms, respectively.

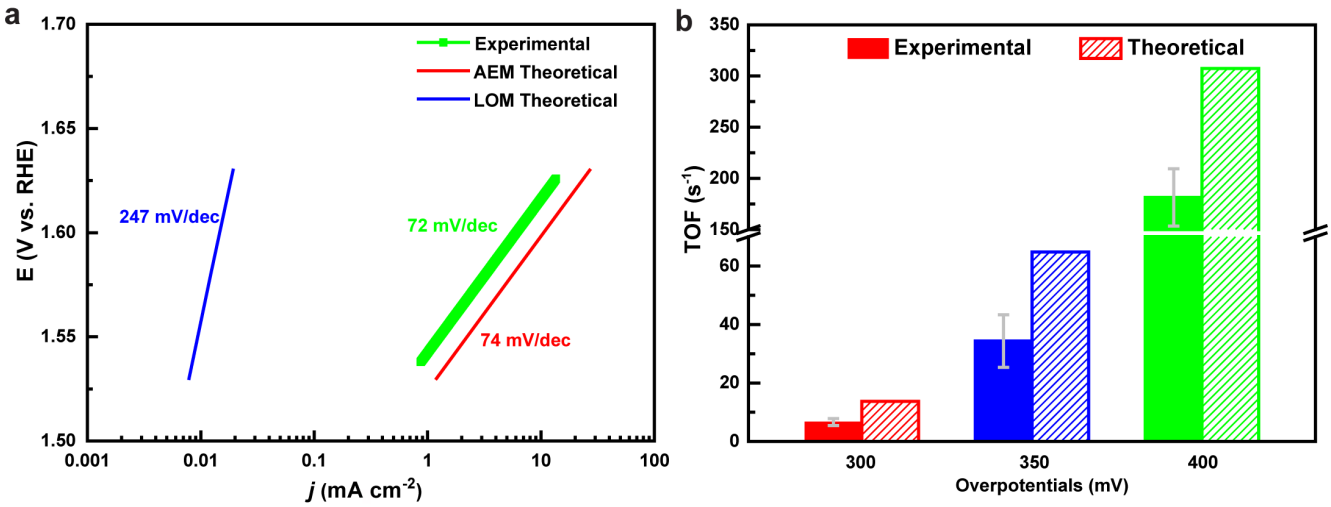

Figure 6. Direct Comparison of experimental results and GCQM predictions. a, Tafel Slope comparison of experimental result, AEM and LOM predictions. The experimental current density of Co-TiO_2 is normalized over ECSA. **b**, TOFs from experiment and GCQM predictions. The predicted TOFs and Tafel Slopes are in excellent agreement with experiment. The error bars represent the standard deviation of experimental TOFs determined from five independent samples.

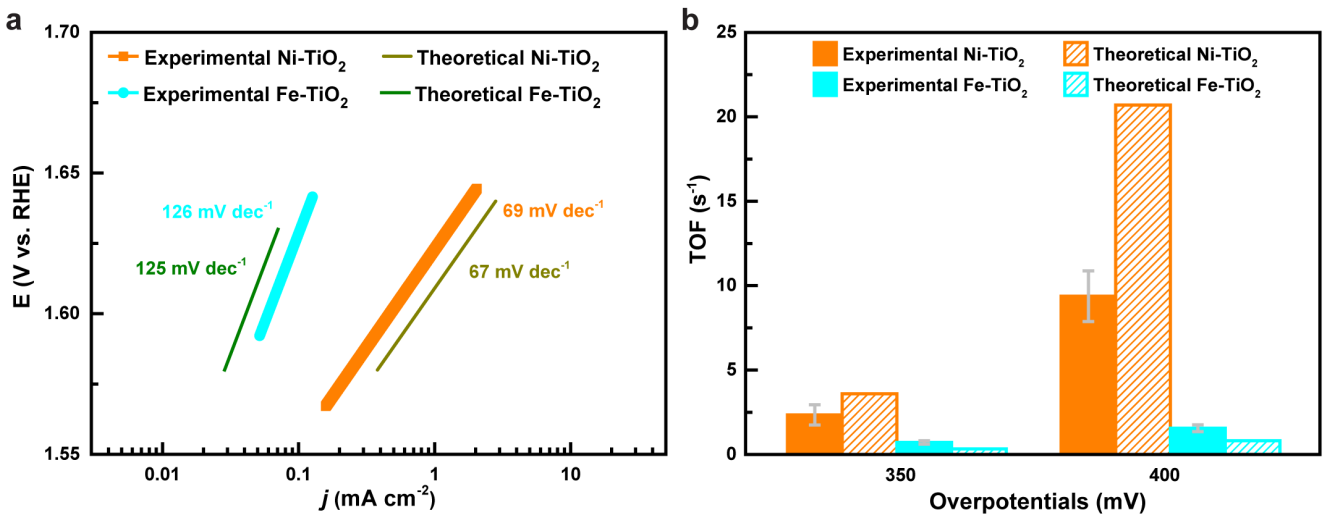

675

676 **Figure 7. Comparison of experimental results and GCQM predictions of Ni- and Fe-TiO_2. a,** Tafel
677 Slope comparison. The experimental current density is normalized over ECSA. **b**, TOFs from experiment
678 and GCQM predictions. The error bars represent the standard deviation of experimental TOFs determined
679 from five independent samples.